very straightforward to extend for pinhole SPECT either due to converging nature of pinhole collimation. To overcome computational problems a relatively simple resolution recovery method for pinhole SPECT was recently presented [16]. This method is based on the use of multi-ray projections, where 7 or 21 projection rays, which intersect the pinhole aperture in a predetermined pattern, are used instead of a single ray going through the pinhole centre. The aim of this work is to compare the multi-ray projection approach to a method with a more accurate model of the acquisition geometry.

Materials and methods

Implementation of the algorithms

The ML-EM algorithm can be presented as

$$\lambda_b^{k+1} = \frac{\lambda_b^k}{\sum_d p(b,d)} \sum_d p(b,d) \frac{n^*(d)}{\sum_{b'} p(b',d)\lambda_{b'}^k} \quad (1)$$

where $\lambda(b)$ is the number of counts emitted from image voxel b, k is the number of iteration, $p(b,d)$ is the probability that the emission in voxel b is detected in detector bin d, and $n^*(d)$ is the measured projection count in detector bin d. The ML-EM algorithm updates the current image estimate using forward projection,

$$\sum_{b'} p(b',d)\lambda_{b'}^k,$$

and back-projection,

$$\sum_d p(b,d) \frac{n^*(d)}{\sum_{b'} p(b',d)\lambda_{b'}^k},$$

operations. In this study three different reconstruction algorithms based on ML-EM and accelerated using the ordered subsets approach were implemented. The first method ($OS\text{-}EM_{noRR}$) used a simple ray-driven forward projector/voxel-driven back-projector pair assuming zero pinhole diameter. The second algorithm ($OS\text{-}EM_{rayRR}$) was implemented using ray-driven forward projection with seven projection rays and voxel-driven back-projector with a single ray. The seven projection rays intersected the pinhole aperture in a hexagonal pattern modelling the effect of the finite pinhole aperture diameter by inverse cone of rays [16]. The third method ($OS\text{-}EM_{psfRR}$) incorporated analytical pinhole collimator point-spread functions into the reconstruction algorithm. The PSFs were calculated according to Metzler *et al.* [17] and stored into hard disk prior to reconstruction in contrast to approach used by the first and second method where the forward projection and back-projection were calculated on-the-fly during the reconstruction.

Phantom studies

The phantom studies were performed using a Toshiba GCA-7200A (Toshiba, Japan) gamma camera equipped with a 251 mm focal length pinhole collimator (0.5, 1.0 and 2.0 mm pinhole apertures specially fabricated for small animal studies). Three phantoms were imaged. The line source phantom consisted of a line source holder and single line source filled with 5 MBq of ^{99m}Tc and placed accurately on the axis of rotation. The resolution was measured as full width at half maximum of horizontal profile taken at the central slice of the phantom. The Jaszczak phantom had four sectors with 1.0, 1.5, 2.0 and 2.5 mm diameter rods separated by a distance twice the rod diameter (Fig. 1). The Jaszczak phantom was filled with 52 MBq of ^{99m}Tc and used to assess the image quality visually. The contrast phantom consisted of eight rods (2.0, 3.0, 4.0, 5.0, 6.0, 7.0, 8.0 and 9.0 mm diameter) and a large background compartment (Fig. 1). The rods were filled with an approximately five times higher concentration of ^{99m}Tc than the background. The total activity in the phantom was 780 MBq. The contrast for each rod was calculated as

$$C = \frac{I_{rod} - I_{bg}}{I_{rod} + I_{bg}} \quad (2)$$

Fig. 1

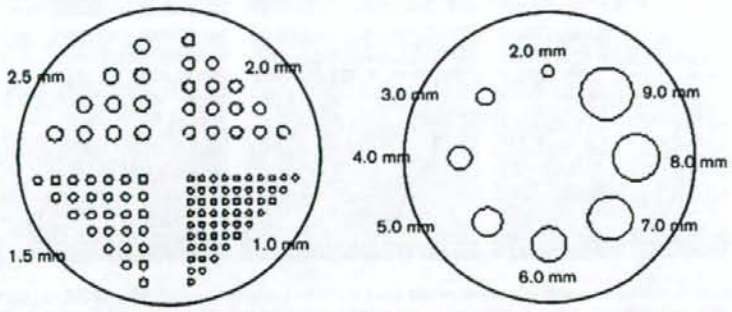

One slice of the Jaszczak phantom (on the left) and contrast phantom (on the right). The phantoms had outer diameter and height of 50 mm. The diameters of the rods are marked on the phantoms.

Table 1 Resolution (measured as full width at half maximum) for 0.5, 1.0 and 2.0 mm pinhole aperture diameters obtained from the line source phantom study, which was reconstructed using OS-EM (five iterations) with the three different resolution recovery methods: no resolution recovery (noRR), multi-ray based resolution recovery (rayRR) and point-spread function-based resolution recovery (psfRR)

	Aperture diameter (mm)		
Algorithm	0.5	1.0	2.0
noRR	1.4	1.6	2.4
rayRR	1.3	1.4	1.3
psfRR	1.2	1.4	1.3

where I_{rod} is the average count in the region of interest (ROI) of the rod and I_{bg} the average count in background ROI. The rod ROIs were circular and had the same diameter as the corresponding rod, whereas each background ROI was annular with inner diameter equal to the diameter of the rod and outer diameter was inner diameter plus 2 mm.

All the acquisitions were performed using 0.5, 1.0 and 2.0 mm pinhole aperture (60° opening angle), 55 mm radius of rotation, 4.3 mm pixel size (128 × 128 matrix), 360° circular orbit and 120 projection angles. In order to avoid centre of rotation shifts the projection data was acquired by rotating the target instead of the detector using the system presented by Zeniya *et al.* [18].

The imaging time per projection angle was selected so that the number of total projection counts was similar in the 0.5, 1.0 and 2.0 mm pinhole aperture studies. The average total projection counts in the line source, Jaszczak and contrast phantom study were 0.9 MCts, 5.2 MCts and 51.8 MCts. The images were reconstructed with the three OS-EM algorithms using eight subsets and five iterations with 0.94 mm voxel size.

Results

Table 1 presents the resolution values after five iterations for the three pinhole apertures and three algorithms. The resolution recovery clearly improves resolution and its effect is more pronounced at larger

Fig. 2

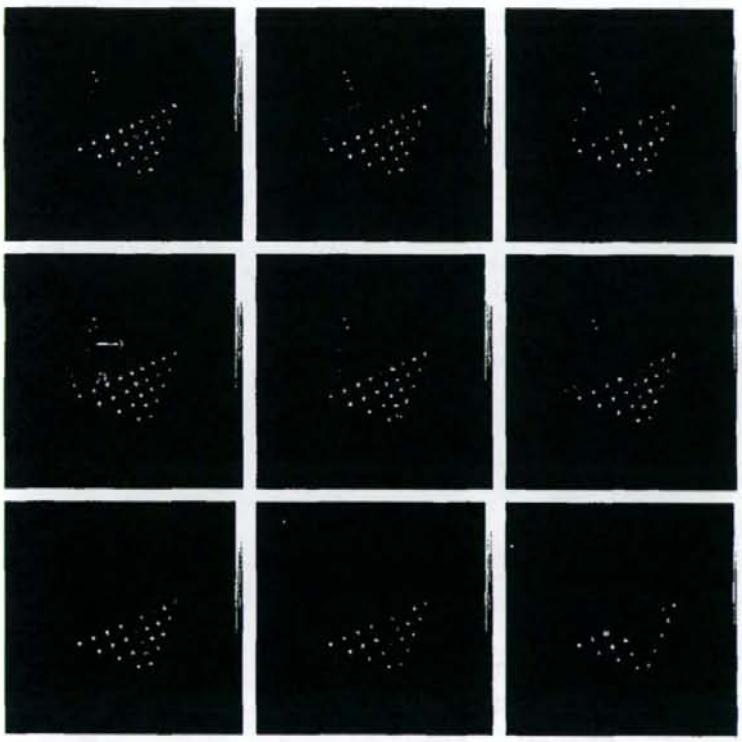

Transverse slices of the Jaszczak phantom study (five slices summed into one); from top to bottom 0.5, 1.0 and 2.0 mm pinhole aperture diameter and from left to right OS-EM with no resolution recovery, multi-ray based resolution recovery and point-spread function based resolution recovery. Air bubbles are marked with arrows on one of the images.

Table 2 Contrast for 0.5, 1.0 and 2.0 mm pinhole aperture diameters obtained from the contrast phantom study reconstructed using OS-EM (five iterations) with the three different resolution recovery methods: no resolution recovery (noRR), multi-ray based resolution recovery (rayRR) and point-spread function based resolution recovery (psfRR)

Rod diameter (mm)	Aperture diameter and resolution recovery method								
	0.5 mm			1.0 mm			2.0 mm		
	noRR	rayRR	psfRR	noRR	rayRR	psfRR	noRR	rayRR	psfRR
2.0	0.34	0.35	0.35	0.29	0.30	0.31	0.13	0.14	0.13
3.0	0.46	0.48	0.50	0.38	0.39	0.41	0.28	0.32	0.28
4.0	0.48	0.49	0.51	0.51	0.54	0.55	0.34	0.40	0.38
5.0	0.48	0.49	0.51	0.49	0.51	0.52	0.37	0.43	0.42
6.0	0.50	0.51	0.53	0.49	0.51	0.53	0.38	0.43	0.41
7.0	0.50	0.50	0.52	0.50	0.53	0.54	0.41	0.46	0.44
8.0	0.49	0.50	0.52	0.48	0.50	0.52	0.39	0.43	0.43
9.0	0.51	0.52	0.53	0.53	0.55	0.57	0.47	0.51	0.49

True contrast of the rods versus background according to Equation 2 is 0.67.

pinhole diameters. On the other hand, the results of the multi-ray and the point-spread function based methods do not differ much. The images of the Jaszczak phantom (Fig. 2) confirm the above findings. The resolution recovery has the biggest effect at the 2 mm pinhole diameter case and the quality of the OS-EM_{rayRR} and OS-EM_{psfRR} images is very similar. The results of the contrast phantom experiment after five iterations are illustrated in Table 2. The methods based on the point-spread function performs slightly better, overall, than does the multi-ray based method.

Discussion

This study compared fast multiple projection ray and analytical point-spread function based resolution recovery methods to uncorrected reconstruction in pinhole SPECT. The multi-ray and point-spread function approaches improved resolution and contrast. The greatest improvement in resolution and contrast was noticed at large pinhole diameters (Tables 1 and 2, Fig. 2). The poor performance of uncorrected reconstruction at larger pinhole diameters is due to the fact that at larger diameters the zero pinhole diameter assumption made in uncorrected reconstruction is violated more than at smaller aperture diameters.

As mentioned in the introduction the biggest problem in incorporating resolution recovery in pinhole SPECT reconstruction is the large computational burden. The calculation time for one iteration of the uncorrected pinhole OS-EM (1.7 GHz Intel processor with 1.0 GB RAM) was 4 min, whereas the computation time for OS-EM_{rayRR} and OS-EM_{psfRR} was 15 min and 10.5 h, respectively, using the acquisition parameters mentioned in the methods section. The reconstruction time of the PSF-based method includes the calculation of the system model, which dominates the calculation time. If the system model for the PSF-based resolution recovery is already stored in a hard disk prior to reconstruction the reconstruction procedure is very fast. Therefore the point-spread function based resolution recovery is suitable for systems where the imaging geometry is fixed [19], because every time the imaging geometry changes, a new system model needs to be generated. The OS-EM_{noRR} and OS-EM_{rayRR}, on the other hand, model the geometry during the reconstruction and can offer clinically acceptable reconstruction times in every case.

The resolution improvement achieved with resolution recovery is important because it allows the use of larger pinhole diameters, which provide higher sensitivity. The poor sensitivity of pinhole collimators has been the biggest problem in small animal pinhole SPECT. Several methods, such as multiple detector heads [3,20] and multiple pinholes [21], have been proposed to overcome this problem, but these approaches require either a multi-headed gamma camera and/or special hardware and are not yet widely applied. Larger injected activities or longer acquisition times are not an optimal approach either, because the radiation burden to the animal or the difficulty of maintaining proper anaesthesia can cause problems. Resolution recovery with a fast resolution recovery algorithm, on the other hand, is almost free of side effects. The only drawback of the multi-ray based approach method is a small increase in noise when compared to reconstruction without resolution recovery, which has been illustrated by Beque *et al.* [16]. The coefficient of variation (COV = standard deviation/mean × 100%) of a large ROI drawn on the uniform background of the contrast phantom also showed this small noise increase. After five iterations the COVs for the 0.5 mm pinhole aperture diameter were 16.1%, 15.4 and 13.7%, when reconstructed with OS-EM_{noRR}, OS-EM_{rayRR} and OS-EM_{psfRR}. The respective values for the 1.0 mm aperture were 16.7%, 17.0% and 14.0%, and 14.6%, 15.9% and 8.4% for the 2.0 mm aperture. The noise properties of the resolution recovery methods were not investigated in detail in this study, because they depended on the implementation of the algorithms. For instance, the noise level of the multi-ray based method

could be decreased by implementing resolution recovery also in the back-projector, but unfortunately this happens at the expense of increased computation time. Noise can also be decreased by using Bayesian reconstruction methods [7], which are almost as fast to execute as the common OS-EM. Therefore from the point of view of the computational burden the best alternative for noise reduction when multi-ray resolution recovery is applied might be to use Bayesian reconstruction methods and model collimator blurring only into the forward projector.

Even though the results presented in this paper were obtained from phantom experiments with activity levels higher than normal can be found in target organs in small animal studies, we are confident that the resolution recovery offers similar improvement in resolution and contrast in small animal studies. However, it is difficult to predict what kind of impact these improvements have, e.g. in brain receptor quantification or measurement of myocardial infarct size in mice and rats. Therefore we plan to further investigate the effect of resolution recovery on (semi-) quantitative values in most frequently used small animal models.

Conclusion

The fast multi-ray resolution recovery method performs almost as well as resolution recovery with accurate point-spread functions and therefore shows promise in improving the resolution–sensitivity trade-off in small animal pinhole SPECT.

Acknowledgement

This work was supported by Japan Society for the Promotion of Science and Nuclear Diagnostics AB.

References

1 Wanet PM, Sand A, Abramovici J. Physical and clinical evaluation of high-resolution thyroid pinhole tomography. *J Nucl Med* 1996; **37**:2017–2020.
2 Bahk YW, Chung SK, Park YH, Kim SH, Lee HK. Pinhole SPECT imaging in normal and morbid ankles. *J Nucl Med* 1998; **39**:130–139.
3 Acton PD, Choi SR, Plossl K, Kung HF. Quantification of dopamine transporters in the mouse brain using ultra-high resolution single-photon emission tomography. *Eur J Nucl Med Mol Imaging* 2002; **29**:691–698.
4 Booij J, de Bruin K, Habraken JBA, Voorn P. Imaging of dopamine transporters in rats using high-resolution pinhole single-photon emission tomography. *Eur J Nucl Med Mol Imaging* 2002; **29**:1221–1224.
5 Habraken JBA, de Bruin K, Shehata M, Booij J, Bennink R, van Eck Smit BLF, Busemann Sokole E. Evaluation of high-resolution pinhole SPECT using a small rotating animal. *J Nucl Med* 2001; **42**:1863–1869.
6 Scherfler C, Donnemiller E, Schocke M, Dierkes K, Decristoforo C, Oberladstatter M, *et al.* Evaluation of striatal dopamine transporter function in rats by *in vivo* beta-[^{123}I]CIT pinhole SPECT. *Neuroimage* 2002; **17**:128–141.
7 Sohlberg A, Lensu S, Jolkkonen J, Tuomisto L, Ruotsalainen U, Kuikka JT. Improving the quality of small animal brain pinhole SPECT imaging by Bayesian reconstruction. *Eur J Nucl Med Mol Imaging* 2004; **31**:986–994.
8 Chatziioannou AF. Molecular imaging of small animals with dedicated PET tomographs. *Eur J Nucl Med Mol Imaging* 2002; **29**:98–114.
9 Meikle SR, Kench P, Kassiou M, Banati RB. Small animal SPECT and its place in the matrix of molecular imaging technologies. *Phys Med Biol* 2005; **50**:R45–R61.
10 Schramm NU, Ebel G, Engeland U, Schurrat T, Béhé M, Behr TM. High-resolution SPECT using multipinhole collimation. *IEEE Trans Nucl Sci* 2003; **50**:315–320.
11 Shepp LA, Vardi Y. Maximum likelihood reconstruction for emission tomography. *IEEE Trans Med Imag* 1982; **MI-1**:113–122.
12 Hudson HM, Larkin RS. Accelerated image reconstruction using ordered subsets of projection data. *IEEE Trans Med Imag* 1994; **13**:601–609.
13 Hutton BF, Lau YH. Application of distance-dependent resolution compensation and post-reconstruction filtering for myocardial SPECT. *Phys Med Biol* 1998; **43**:1679–1693.
14 Yokoi T, Shinohara H, Onishi H. Performance evaluation of OSEM reconstruction algorithm incorporating three-dimensional distance-dependent resolution compensation for brain SPECT: a simulation study. *Ann Nucl Med* 2002; **16**:11–18.
15 Zeng GL, Bai C, Gullberg GT. A projector/backprojector with slice-to-slice blurring for efficient three-dimensional scatter modeling. *IEEE Trans Med Imaging* 1999; **18**:722–732.
16 Beque D, Vanhove C, Andreyev A, Nuyts J, Defrise M. *Correction for Imperfect Camera Motion and Resolution Recovery in Pinhole SPECT.* IEEE Nuclear science symposium and medical imaging conference rome, Italy 2004.
17 Metzler SD, Bowsher JE, Greer KL, Jaszczak RJ. Analytic determination of the pinhole collimator's point-spread function and RMS resolution with penetration. *IEEE Trans Med Imag* 2002; **21**:878–887.
18 Zeniya T, Watabe H, Aoi T, Kim KM, Teramoto N, Hayashi T, *et al.* A new reconstruction strategy for image improvement in pinhole SPECT. *Eur J Nucl Med Mol Imaging* 2004; **31**:1166–1172.
19 Beekman FJ, Vastenhouw B. Design and simulation of a high-resolution stationary SPECT system for small animals. *Phys Med Biol* 2004; **49**: 4759–4792.
20 Ishizu K, Mukai T, Yonekura Y, Pagani M, Fujita T, Magata Y, *et al.* Ultra-high resolution SPECT system using four pinhole collimators for small animal studies. *J Nucl Med* 1995; **36**:2282–2287.
21 Beekman FJ, van der Have F, Vastenhouw B, van der Linden AJ, van Rijk PP, Burbach JP, *et al.* U-SPECT-I: a novel system for submillimeter-resolution tomography with radiolabeled molecules in mice. *J Nucl Med* 2005; **46**:1194–1200.

ELSEVIER

NeuroImage

www.elsevier.com/locate/ynimg
NeuroImage 33 (2006) 1126–1135

Quantitative mapping of basal and vasareactive cerebral blood flow using split-dose ^{123}I-iodoamphetamine and single photon emission computed tomography

Kyeong Min Kim,[a,f] Hiroshi Watabe,[a] Takuya Hayashi,[a] Kohei Hayashida,[b] Tetsuro Katafuchi,[b] Naoyuki Enomoto,[b] Toshiyuki Ogura,[c] Miho Shidahara,[a] Shugo Takikawa,[c] Stefan Eberl,[d] Mayumi Nakazawa,[e] and Hidehiro Iida[a,*]

[a]*Department of Investigative Radiology, National Cardiovascular Center Research Institute, 5-7-1 Fujishiro-dai, Suita City, Osaka, 565-8565, Japan*
[b]*Department of Radiology, National Cardiovascular Center Hospital, Osaka, Japan*
[c]*Department of Neurosurgery, Azabu Neurosurgery Hospital, Sapporo City, Japan*
[d]*Department of Nuclear Medicine, Royal Prince Alfred Hospital, Sydney, Australia*
[e]*Nihon Medi-Physics, Tokyo, Japan*
[f]*Nuclear Medicine Laboratory, Korea Institute of Radiological and Medical Sciences, Seoul, Korea*

Received 17 October 2005; revised 1 March 2006; accepted 25 June 2006
Available online 10 October 2006

A new method has been developed for diffusible tracers, to quantify CBF at rest and after pharmacological stress from a single session of dynamic scans with dual bolus administration of a radiotracer.

The calculation process consisted of three steps, including the procedures of incorporating background radioactivity contaminated from the previous scan. Feasibility of this approach was tested on clinical SPECT studies on 16 subjects. Two sequential SPECT scans, 30 min apart, were carried out on each subject, after each of two split-dose administrations of 111 MBq IMP. Of these, 11 subjects received acetazolamide at 10 min before the second IMP injection. Additional PET scans were also carried out on 6 subjects on a separate day, at rest and after acetazolamide administration. The other 5 subjects were scanned only at rest during the whole study period.

Quantitative CBF obtained by this method was in a good agreement with those determined with PET (y(ml/100 g/min) = 1.07 × (ml/100 g/min) − 1.14, r = 0.94). Vasareactivity was approximately 40% over the whole cerebral area on healthy controls, which was consistent with a literature value. Reproducibility of CBF determined in the rest–rest study was 1.5 ± 5.7%. Noise enhancement of CBF images, particularly the second CBF, was reduced, providing reasonable image quality.

Repeat assessment of quantitative CBF from a single session of scans with split-dose IMP is accurate, and may be applied to clinical research for assessing vascular reactivity in patients with chronic cerebral vascular disease.

Keywords: Split-dose administration; ^{123}I-IMP SPECT; CBF mapping

Introduction

Positron emission tomography (PET) and single photon emission computed tomography (SPECT) are capable of providing physiological functions *in vivo* in a quantitative manner. This is based on mathematical modeling of the kinetic behavior in the body of a tracer that highlights the physiological processes of interest. Two important assumptions are often made, namely, (a) the physiological functions measured are constant over the whole study period, and (b) there is no residual tracer in the body before the tracer administration. These requirements give rise to a crucial restriction in the detection of temporal change of physiological parameters such as cerebral blood flow (CBF). Only a single set of parameters can be determined for a given physiological condition from a series of PET or SPECT measurements. In case of additional assessment at a different physiological condition, an additional scan has to be initiated after decay or excretion of the radioactivity from the body, and the stimulation needs to be applied before the next scan.

One advantage of tracer with a short-lived radioisotope such as ^{15}O in PET is that the radioactivity decays quickly (approximately 2 min half life), which allows a repeat assessment of CBF for several condition within a reasonable interval of typically 10–15 min. However, most PET tracers with longer half-lived radioisotope, such as ^{18}F and ^{11}C, and most SPECT tracers, require background radioactivity compensation, which may be obtained by using the first scan as background or performing an additional image immediately before the second tracer injection. This background subtraction method has been applied to many perfusion studies with SPECT (Hashikawa et al., 1994; Oku et al., 1994; Hattori et al., 1996; Imaizumi et al., 2002), and even to $H_2^{15}O$

* Corresponding author. Fax: +81 6 6835 5429.
E-mail address: iida@ri.ncvc.go.jp (H. Iida).
Available online on ScienceDirect (www.sciencedirect.com).

1053-8119/$ - see front matter © 2006 Elsevier Inc. All rights reserved.
doi:10.1016/j.neuroimage.2006.06.064

PET studies (Chmielowska et al., 1998; Chmielowska et al., 1999). The subtraction method, however, degrades the image quality and quantitative accuracy. A tracer that shows clearance or limited retention in the tissue requires minimizing the scan period for the background not to affect the parameter estimation in the second scan, but this results in the degraded image quality. In turn, a prolongation of the background scan, intended to prevent degrading image quality, causes inconsistency with the parameter estimation due to the time-dependent distribution of the tracer in the next. Clearance of the tracer from tissue is observed not only in the PET study using $H_2^{15}O$ but also in several SPECT studies, such as ^{123}I-iodoamphetamine (IMP) for quantitation of CBF (Iida et al., 1994a,b).

For repeat CBF studies in a single session, we have presented a new mathematical formulation to compensate for the background radioactivity contamination in tissue from the tracer previously administered (Iida et al., 2000; Nishizawa et al., 2003). This allows estimation of "snapshot"-like background radioactivity distribution just before the second tracer scan from the information obtained from whole the previous scan data assuming a compartment model. This background distribution was then built into a model for the parameter estimation using the second tracer data. Based on this formulation, we demonstrated the applicability of this approach to repeat CBF measurement using $H_2^{15}O$ PET in a shorter interval (Watabe et al., 2002).

In this study, we have aimed to make the CBF images of repeat SPECT scan, based on the above formulation, and to evaluate the validity and applicability of this functional mapping method by means of clinical studies performed with SPECT and IMP. Quantitative accuracy of this method was also tested by comparing CBF values with those in $H_2^{15}O$ PET studies.

Materials and methods

Theory

The new mathematical approach, Dual-Table autoradiography (ARG) method was formulated for a cerebral perfusion tracer, which has high trans-capillary extraction to the cerebral tissue with significant clearance. IMP has been chosen in this study. It was assumed that the kinetics of this tracer follows a single-tissue compartment model (Kuhl et al., 1982; Iida et al., 1994a, b). The calculation of CBF at baseline and after the pharmacological stress included three processes as shown in Fig. 1. The first process calculates a CBF (f_1) map from an early image obtained immediately after the first tracer administration based on a previously validated *in vivo* autoradiography technique for IMP, by employing a lookup table procedure (Fig. 1A) (Iida et al., 1994a,b; Iida et al., 1996). The second process estimates a background radioactivity distribution immediately before the next injection of IMP, using the CBF image obtained from the first process (Fig. 1B). This is an inverse procedure of the first process, but estimates the momentary ("snapshot"-like) radioactivity distribution at the time of the second IMP injection. The third process then calculates a CBF (f_2) map after the pharmacological stress from the next early image in addition to the background image generated by the second process (Fig. 1C). For this calculation, the tissue radioactivity concentration was formulated as follows;

$$\int_{T_1}^{T_2} C_t(t)\mathrm{d}t = f_2 \cdot \int_{T_1}^{T_2} C_a(t)c \otimes e^{-\frac{f_2}{V_d}\cdot t}\mathrm{d}t + C_t\left(T^{bkg}\right) \cdot \int_{T_1}^{T_2} e^{-\frac{f_2}{V_d}\cdot\left(tt - T^{bkg}\right)}\mathrm{d}t \quad (1)$$

where $C_t(t)$ is regional tissue radioactivity concentration (cps/g) in the next early image at time t, f_2 CBF (ml/min/g) after the pharmacological stress, V_d distribution volume of the tracer (ml/ml), T_1 and T_2 the scan start and end times for the second scan, respectively, T^{bkg} is the time defined for the background activity before T_1, $C_a(t)$ arterial input function (cps/g), and $\otimes$ convolution integral, respectively. The first-pass extraction fraction is assumed to be unity and independent of time.

The lookup table process therefore includes two tables (see Fig. 2), namely response to the second tracer administration (the first term in the right of Eq. (1)) and the contribution of remaining radioactivity (the second term in the right of Eq. (1)). The second table is scaled by the background counts, $C_t(T^{bkg})$.

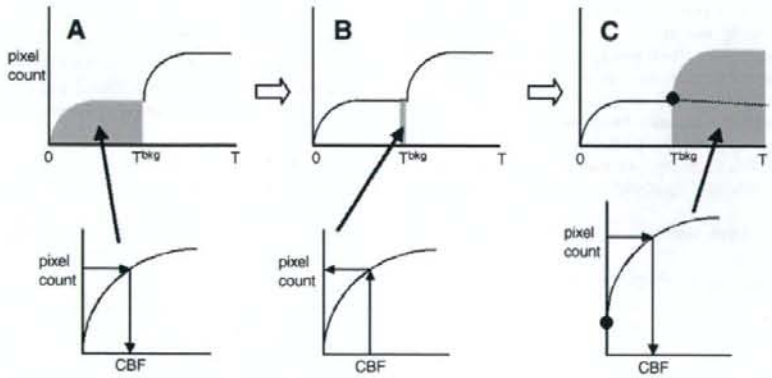

Fig. 1. Mathematical procedure to estimate the first and second CBF maps from a series of SPECT scans following split-dose administration of IMP. The calculation process consists of three steps, namely, (A) calculation of a baseline CBF map from the early image according to the IMP autoradiography, (B) estimation of a transient radioactivity distribution at the end of the scan (or at the time of the next scan initiation) from the CBF map, and (C) calculation of additional CBF map from the second SPECT image. Note that the estimated background distribution is implemented in the model formulation of the second CBF calculation process. Pharmacological stress can be given prior to the second IMP administration in a typical clinical study.

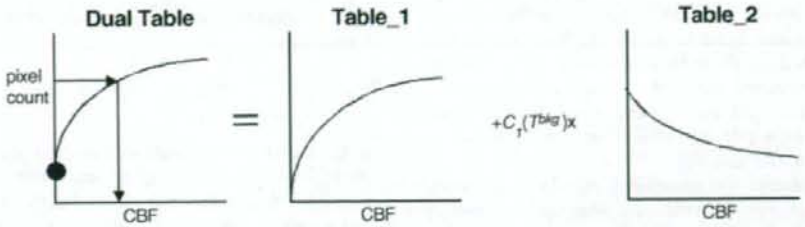

Fig. 2. The procedure to estimate the CBF map from the second SPECT scan. Once a table between CBF and SPECT counts is generated, a lookup table procedure provides a CBF map from pixel counts of the second SPECT image. This table is the sum of two tables corresponding to each term of Eq. (1). The first component corresponds to the response to the newly supplied tracer, and the second table corresponds to the contribution of background activity. Note that the second table is scaled in each pixel by referring the background radioactivity counts at the time of the second scan initiation, which are generated from the previous CBF map.

It is likely that CBF varies during the scan, particularly when pharmacological challenge is given before the end of the first scan. With the definition of a transient weight function, $w(t)$, describing effects of the transient CBF change on the estimated background radioactivity that should be used in the next CBF calculation, the observed tissue concentration, $C_i(T)$, is expressed with $w(t)$ and the transient CBF or $f(t)$ as (Iida et al., 1991);

$$C_i(T) = \int_0^T w(t) f(t) dt \tag{2}$$

With assuming a two-compartment model for a constant f during the study and differentiation, $w(t)$ can be approximated by;

$$w(t) \approx \frac{dC_i(t)}{dt} \tag{3}$$

Thus the transient weight in the estimated background image is nearly equal to the first derivative of the tissue concentration curve during the previous scan. This suggests that the estimated background distribution for the next scan is predominantly sensitive to flow during the rising period following the bolus injection of IMP, and is only moderately affected by flow after a certain period has elapsed from the previous scan. Thus, minimal effects are expected in the background estimation process, even when pharmacological stress is applied before end of the previous scan.

Subject

Studies were performed on subjects. Subjects were divided into 3 groups. The first group ($n=5$) was consisted of clinical patients with cerebral ischemia, who were assigned to the IMP SPECT studies for clinical diagnosis, and were used to evaluate the reproducibility of the method. In this group, patients were scanned at rest during the whole study period (rest–rest condition). Their age ranged from 51 to 71 years old (mean±SD; 61±9). Four patients suffered from chronic cerebral hemorrhage, and one had an unruptured aneurysm.

The second group consisted of only healthy male volunteers ($n=5$), who had no signs or symptoms of stroke or other ischemic diseases, and were expected to show normal range of CBF values. All subjects belonging to this group were studied at rest during the first scan, but acetazolamide (ACZ) was administrated before the second IMP injection (rest-ACZ condition). Their ages ranged from 27 to 35 (mean±SD; 30±4).

The third group included 6 patients with stenosis or occlusion of extracranial internal carotid artery on unilateral ($n=3$) or bilateral ($n=3$) side. Their age ranged from 71 to 74 years old (mean±SD; 72±1). All patients underwent the IMP SPECT scans at rest and with an acetazolamide challenge, as in the second group, and PET scans following intravenous ^{15}O–water both at rest and after the same dose of acetazolamide, were done 2 days apart from the SPECT study with acetazolamide challenge. The second scan data of one subject among the subjects in this group, were excluded in the data analysis, because of the severe head motion and urination during SPECT acquisition.

All subjects had MRI scans prior to the SPECT study, which has been used for identification of region-of-interest (ROI) and also for generating attenuation maps that have been utilized for corrections of attenuation and scatter in the SPECT reconstruction (see below). All subjects gave written informed consent, and were studied by the protocol approved by the local ethical committee.

SPECT scan

All SPECT studies were carried out following the split-dose administration of IMP. For the first and the second groups, a triple-headed SPECT camera attached with low-energy high-resolution fan-beam collimator (GCA-9300A, Toshiba Medical System, Tokyo, Japan), installed at Azabu Neurosurgery Hospital, was used. And a dual-headed gamma camera attached with low-energy high-resolution fan-beam collimator (ECAM, Siemens Medical System, USA), installed at National Cardiovascular Center Hospital was used for the third group. The size of acquired projection was 64-by-64 pixels, and the energy window selected was 20% on the center of 159 keV for all studies.

In each subject, the split-dose IMP injections (111 MBq each) were separated by an interval of 30 min. The infusion period was 1 min, and was controlled using a constant infusion pump (Terumo, Tokyo, Japan). Two sets of dynamic SPECT scans were initiated at the time of the IMP injection. The duration of each dynamic scan was 30 min for the 1st and 2nd groups and 25 min for the 3rd group, respectively. For both SPECT scans, the detectors were rotated continuously collecting 60 projections over 360° initially every 10 s and, after 5 min, every 2 min for the triple-headed camera, and initially every 2 min and, after 10 min, every 5 min for the dual-headed camera. The acquired projection data

were re-binned to parallel beam projection for further process. Each dynamic projection data with the parallel-beam transformation were summed to a static data for each session, and two sets of images were reconstructed for further image calculation (see below). In the second and third groups, 16 mg/kg (1000 mg maximum) of acetazolamide was administered intravenously at 20 min after the first IMP injection.

Arterial input function was determined in individual studies. Arterial blood was sampled from the radial artery at 15-s intervals during the first 2 min with gradual prolongation thereafter. The whole blood radioactivity concentration was counted using a well counter, and its octanol extraction fraction was also counted as reported previously (Kuhl et al., 1982; Lear et al., 1982; Kurisu et al., 2002).

A uniform cylindrical phantom of 16-cm diameter (axial length of 15 cm) filled with approximately 20 MBq of ^{123}I-solution was scanned following the same scan protocol as for the clinical SPECT studies. The solution was sampled and its radioactivity concentration was counted in the well counter that was used for measuring the arterial blood radioactivity concentration.

PET scan

Six subjects belonging to the third group underwent a series of PET scans within 2-day period from the IMP study. The ECAT Exact47 PET scanner (Siemens-CTI Inc., Knoxville, USA) was used, which provides 47 tomographic slices. The observed spatial resolution of reconstructed image was approximately 7-mm FWHM both in-plane and in axial direction.

After a transmission scan for attenuation correction, a 90-s scan was performed following a bolus injection of ^{15}O-labeled water ($H_2^{15}O$). The functional CBF images were calculated according to the $H_2^{15}O$ autoradiography (ARG) technique (Kanno et al., 1987). The partition coefficient of water was assumed to be 0.80 ml/g, which was meant to minimize effects of tissue heterogeneity (Iida et al., 1988). The arterial input function was determined from the continuously monitored arterial blood time–activity curve including corrections for delay and dispersion (Iida et al., 1986, 1989). The scans were performed twice, the first at rest, and the second at 10 min after administration of the same dose of acetazolamide as in the SPECT study.

SPECT image reconstruction

To generate uniform attenuation map by means of MRI image, both static projections of the first and second sessions were reconstructed without correction of attenuation or scatter, to provide SPECT images for each session, and MRI image of each subject was co-registered to the reconstructed image without attenuation correction, using SPM2 (Welcome Department of Imaging Neuroscience, University College London, London, UK). The co-registered MRI image was converted to an attenuation map, after defining the head contour and assigning a value of uniform attenuation coefficient of 0.167 cm^{-1} into the area inside the head contour (Iida et al., 1998). The uniform attenuation map was used in image reconstruction with corrections of attenuation and scatter. Scatter component in emission projection was corrected by employing a technique of transmission-dependent convolution subtraction (TDCS), as previously validated (Meikle et al., 1994; Narita et al., 1996; Iida et al., 1998). The TDCS can provide the pixel-by-pixel estimation, $k(x, y)$, of scatter component in measured emission data, by means of the following formulation;

$$k(x,y) = 1\frac{1}{A - B \cdot t(x,y)^{\beta/2}} + k_0 \quad (4)$$

where $t(x, y)$ is an attenuation factor for pixel (x, y) and k_0 is a term illustrating both septal penetration and scatter in the collimator due to contamination of high-energy photon of ^{123}I. The parameter sets for TDCS are A=2.4718, B=$A-1$, β=0.2088, and k_o=0.2141 for the triple-headed camera, A=2.3069, B=$A-1$, β=0.2926, and k_o=0.3000 for the dual-headed camera, respectively. These parameters were empirically determined by the previous study (Kim et al., 2001). The scatter-corrected projections were then reconstructed using the in-house package for quantitative SPECT reconstruction (QSPECT), which employed the ordered-subset expectation maximization (OS-EM) algorithm including the attenuation correction with the attenuation map (Hudson and Larkin, 1994). The reconstructed images were then cross-calibrated to the well counter system using the cross-calibration factor determined as below.

Images of the cylindrical phantom were reconstructed following the same procedures as for the clinical study, including correction for scatter and attenuation. A circular region-of-interest (ROI) of 8-cm diameter was placed on the transverse image, and mean counts over this ROI were referred to the radioactivity concentration of this solution (cps/g) measured by the well counter. The ratio of these two values was defined as the cross-calibration factor between the SPECT and the well counter system.

Data analysis

The reconstructed images of the first and second session were realigned using SPM2, to correct a possible head motion between both scan sessions. Quantitative CBF images were calculated for both the first and second SPECT images, respectively, as described in the theory, with setting T^{bkg} to T_1. The distribution volume of IMP, V_d, was fixed at 35 ml/ml in the CBF calculation (Hatazawa et al., 1997; Iida et al., 1998). The image of background radioactivity generated during CBF calculation was compared with the reconstructed image immediately before the second IMP injection, i.e., the image with scan duration of 20–30 min for the first and second groups, and 20–25 min for the third group, respectively. All calculated CBF images of SPECT and PET were co-registered to its own MRI image, using SPM2.

In total, 39 circular ROIs with 2 cm of diameter were placed on MRI image, to cover the whole brain according to the criteria described elsewhere (Yamaguchi et al., 1986; Iida et al., 1998). These ROIs were projected on all CBF images to investigate the reproducibility between the first and second scans, and the consistency of the proposed method with PET. The rest–rest study was used to evaluate the reproducibility of the estimated CBF values between the two sessions, while the rest–acetazolamide study was used to evaluate the vasareactivity in normal subjects (namely the second group). Consistency of the calculated CBF values between the present method and PET was also evaluated.

All data were presented as mean ± SD, and Pearson's correlation and linear regression analysis were used to evaluate relationships between the two CBF values. The reproducibility of both measured and estimated background images was evaluated by means of Mann–Whitney rank sum test.

Results

Figs. 3A–C show a comparison of the background radioactivity concentration at 25 min after the first IMP injection estimated by the present model-based approach, with those obtained from a scan with short duration. Fig. 3A is a typical comparison of the background images obtained from one study among the first group. It appears that the estimated images show visually smoother, therefore smaller noise, than the measured images, while the absolute counts are equivalent. ROI counts of the estimated background images were also compared with those of the measured images for the rest–rest studies of the 1st group and the rest–acetazolamide studies of the third group in Figs. 3B and C, respectively. There is no significant difference between the two methods both in the rest–rest ($p>0.5$) and rest–acetazolamide ($p>0.1$) studies. However, the rest–acetazolamide study indicated slightly greater spread about the regression line.

Fig. 4A shows comparison of CBF images obtained from one of the rest–rest studies, indicating the reproducibility of the CBF measurement by the present method (Dual-Table ARG method). The visual difference between the estimated and measured background images in Fig. 3A leaded to the similar quality between the first and second CBF image set, although there is some difference in noise between test and retest. It is clear that the quantitative values of CBF are consistent between the two CBF images obtained from the first and second scans (see also Fig. 4B). The reproducibility between the two CBF values obtained from the rest–rest study as evaluated as a deviation of the two averages between the first and second CBF values was 1.5±5.7%. There was no significant difference between them.

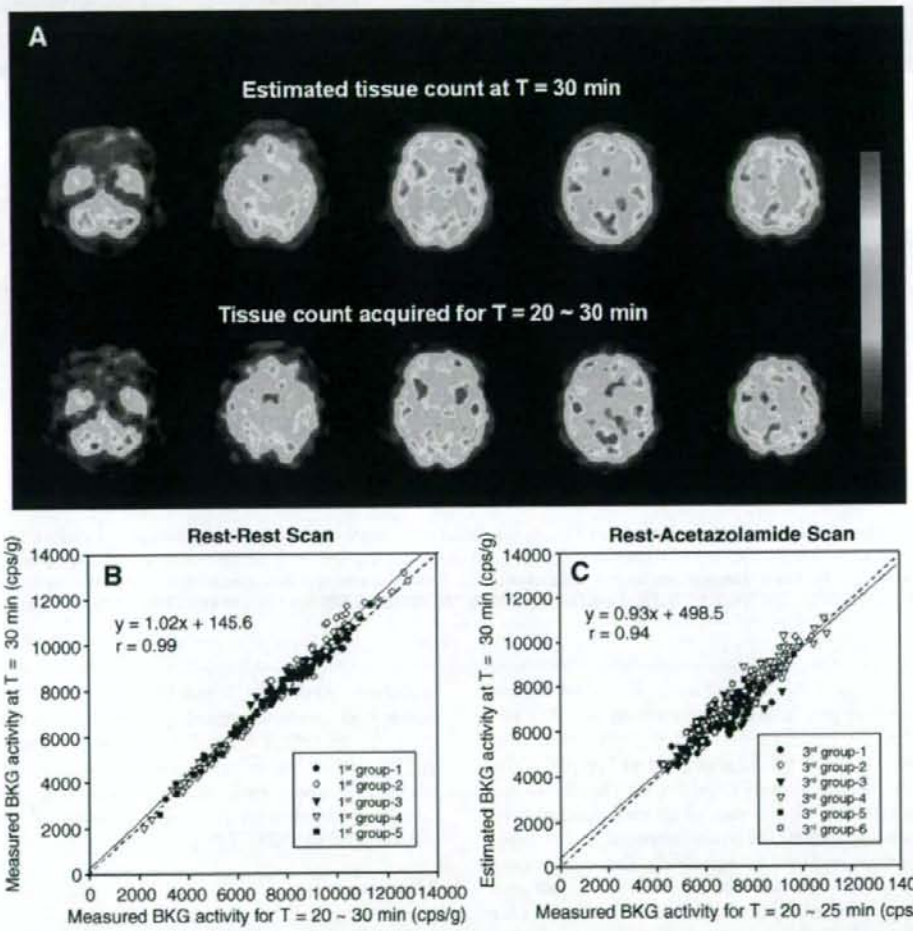

Fig. 3. (A) Comparison of background images estimated by the proposed method (top) with those acquired by a 10-min scan (t=20–30 min) with the triple-headed camera. (B) Comparison of pixel counts estimated by the proposed method with those acquired by a 10-min scan with the triple-headed camera. Values were obtained from 39 circular regions of interest that had a size of 314 mm^2. Data are obtained from the rest–rest studies (n=5), and regression lines are plotted for each subject. (C) Same as for panel (B) but from the rest–acetazolamide studies, in which background activity was compared with those by a 5-min scan (t=20–25 min) with dual-headed camera.

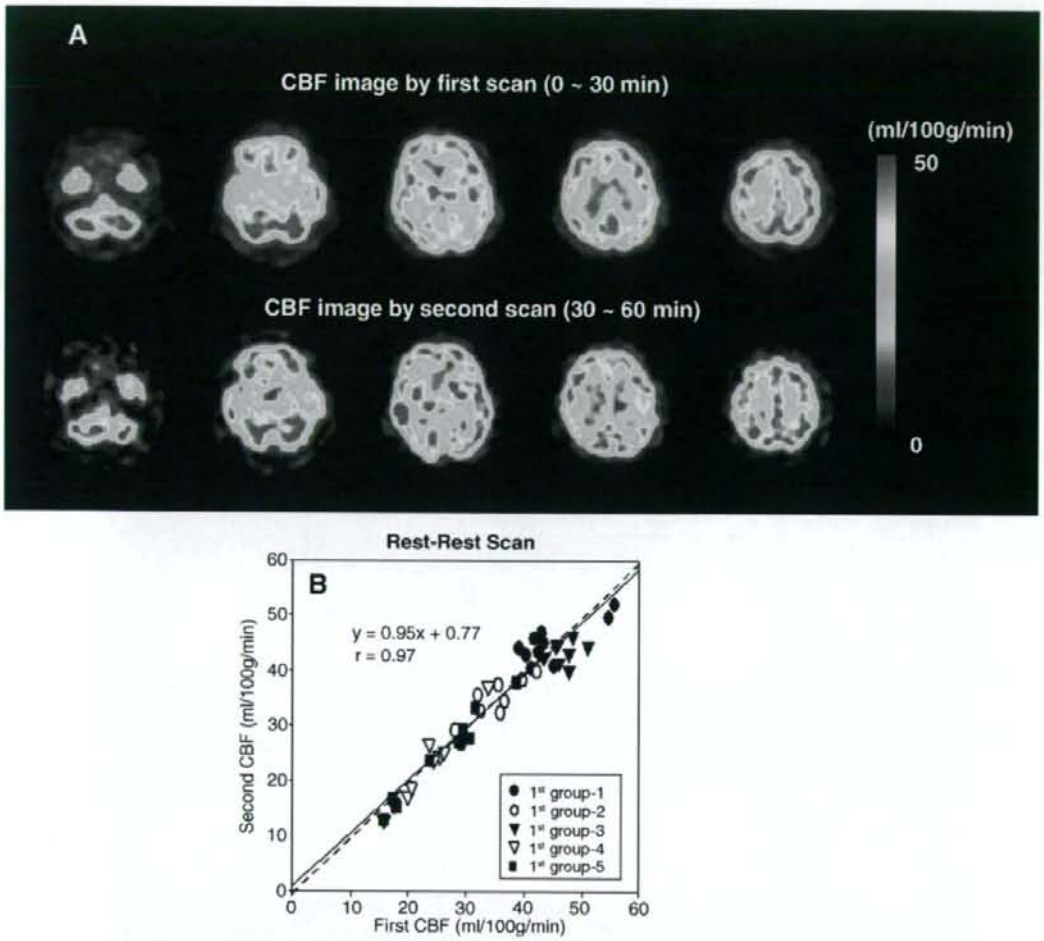

Fig. 4. (A) A comparison of calculated CBF images obtained from a typical clinical study with the rest–rest protocol. CBF images are shown for both first (top) and second (bottom) scans, demonstrating reproducibility of the method. All images are displayed with the same color scale in units of ml/100 g/min. (B) Comparison of calculated CBF values obtained from the rest–rest studies ($n=5$). Each value corresponds to a mean value of regions of interest in each area of deep and cortical gray matter (frontal, temporal, occipital gyri) and cerebellum. No significant difference was observed between the first and the second CBF values.

In the second group, CBF values of three gray matter regions (e.g., cortical and deep gray matter and cerebellum) were 37.4 ml/100 g/min, 36.4 ml/100 g/min, and 44.4 ml/100 g/min for rest state, and 53.1 ml/100 g/min, 51.5 ml/100 g/min, and 63.7 ml/100 g/min for acetazolamide state, respectively (Figs. 5A, B). The CBF values of whole region including white matter, which were obtained from the 39 ROIs, were 37.1±5.0 ml/100 g/min for rest and 52.2±8.0 ml/100 g/min for acetazolamide states, respectively. These CBF values resulted in the global CBF increase of 40.5±9.4%, and was homogeneous in all cerebral regions (43.0% for cortical, 42.3% for deep gray matter and 39.4% cerebellum). This increase of 40% agreed with the literature value (Hayashida et al., 1996). No significant difference in the amount of increase was observed among the regions (see Fig. 5B).

Figs. 6A–C show the results of comparison of rest–acetazolamide studies with SPECT and PET. The CBF images by both the Dual-Table ARG SPECT and $H_2^{15}O$ ARG PET methods were similar both quantitatively and qualitatively (Fig. 6A). The CBF values by the SPECT method showed the consistency with those by PET over the regions of deep and cortical gray matter (frontal, temporal, occipital gyri) and cerebellum (Fig. 6B), and this consistency resulted in the good correlation of CBF increase between PET and SPECT (Fig. 6C).

Discussion

In this study, we developed a new method of quantitative CBF mapping, which is based on the mathematical formulation for repeat CBF quantitation using a diffusible tracer that incorporates time-dependent changes of tissue radioactivity distribution, and showed that this method allows the test–retest assessment of quantitative CBF images within a reasonable scan

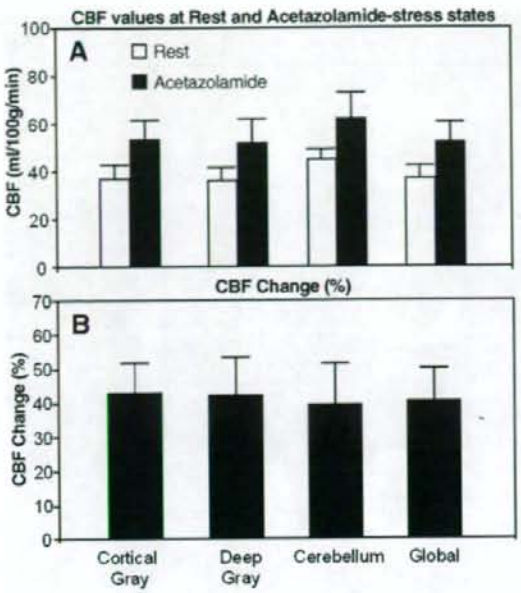

Fig. 5. (A) CBF values at both of rest and acetazolamide-stress states and (B) %change of CBF obtained from the rest–acetazolamide studies performed on the second group. The values of CBF and %change of three gray matter regions, namely the cortical and deep gray matter and cerebellum, and the whole brain regions, were summarized. No significant difference was observed in the %change among the regions.

interval. The noise enhancement, which has been a major restriction in previous approaches when using a simplified background subtraction technique, has been suppressed with the present approach.

Validity of this method has been demonstrated in sequential SPECT studies at rest and after acetazolamide in conjunction with a split-dose administration of IMP. IMP is a diffusible tracer with significant clearance from the brain over time (Kuhl et al., 1982; Iida et al., 1994a,b). It should, however, be noted that the kinetic behavior of IMP can be well described by a mathematical model (single-tissue compartment model). Thus, in this study, the formulation was given, based on the single-tissue compartment model, for a split-dose administration protocol, allowing the accurate quantitation of CBF at two physiological conditions. The quantitative accuracy and the precision of this approach at rest and after acetazolamide are acceptable in the clinical setting, allowing the rest–acetazolamide study to be carried out with a total study time of less than 1 h with an interval of 20 to 30 min between the two IMP administrations.

The new formulation that estimates the second CBF from the second SPECT scan by incorporating the background radioactivity from the previous scan into the formulation, has been validated successfully in this study with clinical scans. The calculated CBF images were consistent between the first and the second scans in the rest–rest study, in which image quality of the second CBF was not different from that from the first scan. In the previous work (Iida et al., 2000), we have evaluated the reproducibility of both CBF image in rest–rest study, using 160 square ROIs (34×34 mm^2) those were placed on brain region including gray and white matter of 5 tomographic slices of CBF images at axial position shown in Figs. 3A and 4A, and obtained the difference within 3%. In other study presented in domestic meeting (Annual meeting of Japanese Society of Nuclear Medicine (2000)), we have also compared the test–retest CBF image sets generated in rest–rest study by the presented method, with those by a traditional microsphere method (Kuhl et al., 1982), and found same reproducibility of the both test–retest CBF images for the both CBF calculation methods, with better quality of the second CBF image by the presented method than by the traditional method. Therefore, from these previous results showing enough accuracy of reproducibility over whole brain regions, we have focused the variation of CBF values in regions those have been interested in many clinical studies, rather than whole brain regions. The rest–acetazolamide study also demonstrated reasonable quality of CBF images both at rest and after acetazolamide. The estimated values of CBF at both rest and acetazolamide states, and %increase of CBF showed a good linear relationship with those by $H_2^{15}O$ PET, although there was a small offset in the comparison of %increase of CBF. This small bias was resulted from the slight underestimation of background radioactivity, which might be affected by reconstructed image with lower count statistics due to the fewer number of detector and relatively higher scatter fraction in the data acquired from dual-headed camera, compared to that of triple-headed camera ($k_0 = 0.3000$ for dual-headed and $k_0 = 0.2141$ for triple-headed). The amount of about 40% increase of CBF in healthy volunteers, however, agreed with the literature values, which also suggests validity of the present method (Hayashida et al., 1996).

The transient distribution of the tissue radioactivity concentration at the time of the second IMP injection can be accurately estimated from the first scan with the present method with minimal enhancement of statistical noise. It was shown that this estimated tissue radioactivity distribution was in a good agreement with that directly measured by a short (10 min or 5 min) SPECT scan, without enhancement of statistical noise (Fig. 3A). It is important to note that this agreement was confirmed not only in the rest–rest protocol (Fig. 3B), but also in the rest–acetazolamide protocol (Fig. 3C), in which the acetazolamide challenge was given during the 1st SPECT scan. This can be understood by referring to the approximate formulation of the transient contribution weight as defined in Eq. (3). As has been described in theory, the transient contribution is approximately proportional to the first-derivative of the tissue radioactivity concentration, and thus highly weighted only at the early phase after the tracer administration, but small after the peak of tissue radioactivity when a bolus administration protocol in employed. CBF changes some time after the immediate period post IMP injection have only a very small or negligible effect on the background activity. Eq. (2) also implies that the estimated CBF maps at rest and after acetazolamide are highly weighted to the early period immediately after each of IMP administrations, which has been shown in the previous study using simulation (Iida et al., 2000). From these findings, it can be expected that the second CBF should yield the elevated CBF values even though CBF is decreased after a certain period such as >10 min after the 2nd IMP administration.

In general, kinetic analysis in PET or SPECT assumes a constant physiological condition throughout the whole study period, and only a single set of physiological parameters such as CBF is typically estimated from a series of data. The temporal resolution of the PET/SPECT methodology has therefore been

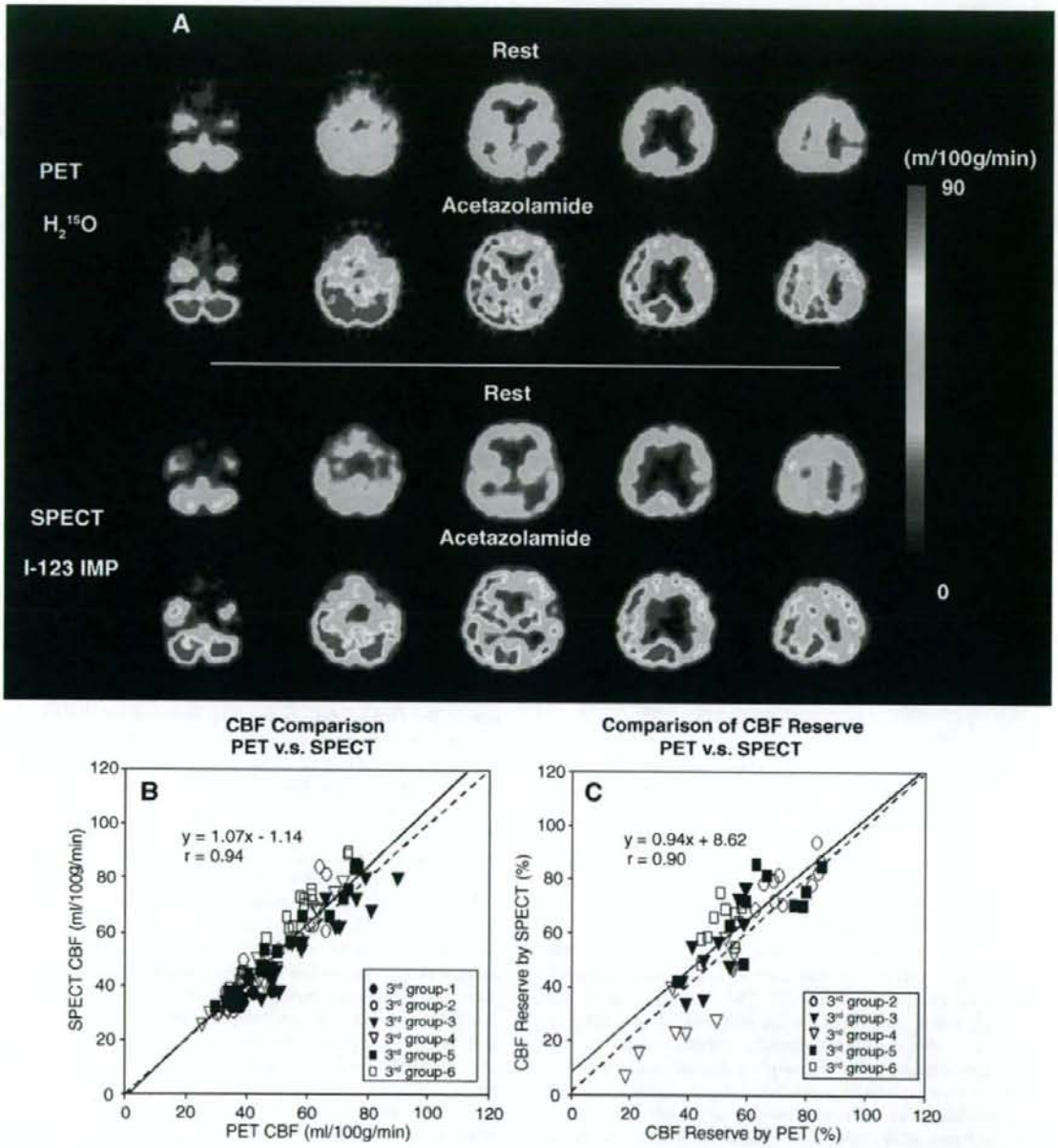

Fig. 6. (A) A comparison of calculated CBF images obtained by PET (top two) and SPECT (bottom two) from a typical clinical study with the rest–acetazolamide protocol. CBF images are shown for both first (first and third rows) and second (second and forth images) scans, respectively, and reveal that the present method is comparable with that by PET in CBF estimation. CBF images obtained by the present method (bottom two) were also compared with those (top two) by the conventional $H_2^{15}O$ ARG PET. All images are displayed with the same color scale in units of ml/100 g/min. (B) Comparison of calculated CBF values obtained from the rest–acetazolamide studies with dual-headed camera and PET ($n=6$). Each value corresponds to a mean value of regions of interest in each area of deep and cortical gray matter (frontal, temporal, occipital gyri) and cerebellum. (C) Comparison of %increase of CBF values calculated with the CBF values of (B). %Increase of CBF was calculated by $([\text{CBF(acetazolamide)}/\text{CBF(rest)}]-1)\times 100$.

restricted by this limitation. It is, however, important to note that the CBF estimated by the present method was highly weighted by the transient CBF for a certain period. This contribution of transient weight in the estimated CBF has been discussed already in previous publications for $H_2^{15}O$ PET ARG (Iida et al., 1991), and this has been applied to cognitive activation studies to detect 30-s

momentary change (Silbersweig et al., 1993, 1994). All of these findings support the validity of the present Dual-Table ARG approach for estimating CBF maps with the split-dose administration of IMP.

The evaluation of rest–acetazolamide CBF was a goal of the application of this methodology. This is based on the on-going project in Japan, which re-evaluates the previous reports regarding the value of extracranial/intracranial arterial anastomosis in patients with symptomatic occlusive disease of the internal carotid artery (Vortrup et al., 1984; The-EC/IC-Bypass-Study-Group, 1985a,b; Vortrup et al., 1986). The previous study failed to show significant efficacy of the bypass surgery, but it did not selected patients by the aid of information for cerebral hemodynamics using functional imaging. The on-going project is intended to select only the severely ischemic patients (Stage II ischemia) by means of evaluating the reduced baseline CBF with a lack of vasareactivity after acetazolamide challenge (Powers, 1991; Hayashida et al., 1996, 1999). PET is able to provide useful information (Powers and Raichle, 1985), but due to its limited availability in clinical centers, this Dual-Table ARG approach with IMP and SPECT may be of use for this project. A further evaluation is needed to confirm this.

The present Dual-Table ARG method may be applied to other tracer studies. Chmielowska et al. (1998, 1999) claimed that the qualitative CBF mapping during cognitive activation may be obtained with a 6-min interval by involving a simple background subtraction, yielding consistent activation foci as compared with a traditional protocol based on repeat PET scanning with repeat $H_2^{15}O$ injection at 10- to 12-min interval. DT-ARG approach to various tracer studies was evaluated by simulation (Iida et al., 2000), in which dual bolus administration and transient CBF change were simulated with assumption of $V_d=28$ for IMP and $V_d=0.8$ for $H_2^{15}O$, respectively. The simulation demonstrated that the increased CBF is estimated only when the true CBF was increase at the extremely early phase after the administration of IMP or $H_2^{15}O$, while the second CBF was independent of the change of CBF during previous scans in the both IMP and $H_2^{15}O$ simulations. Application of the present Dual-Table ARG approach to the $H_2^{15}O$ PET activation study may be able to further shorten the scan interval (approximately 1.5 min) (Watabe et al., 2002), by incorporating the background radioactivity distribution into the kinetic model formulation. Another possibility is the quantitative $CMRO_2$ study by means of PET scans following sequential administration of $^{15}O_2$ and $H_2^{15}O$. The previous protocol proposed by Mintun et al. (1984) was based on independent three step measurements following each of the $C^{15}O$, $^{15}O_2$ and $H_2^{15}O$ administration. The present approach, with the help of the estimated background radioactivity distribution in the sequential administration, could reduce the intervals between the scans without the loss of quantitative accuracy and image quality of each functional images of $CMRO_2$ and CBF, respectively, in anesthetized monkey study (Kudomi et al., 2005). Systematic studies are obviously needed in order to evaluate the feasibility of this technique in clinical studies.

We have previously demonstrated the importance of accurate image reconstruction in SPECT and employed a novel program package in order to achieve accurate reconstruction. Scatter, which was shown to cause serious reduction of the image contrast between the high CBF and low CBF areas, was corrected by the previously validated TDCS method (Meikle et al., 1994; Narita et al., 1996; Iida et al., 1998) together with correction for the penetration from the high-energy contamination (Kim et al., 2001). The photon attenuation correction was included in the OS-EM reconstruction procedure by using the attenuation map that was estimated from the head contour of its own MRI image (Iida et al., 1998). Details of the procedures and their validation have been described elsewhere (Iida et al., 1998; Kim et al., 2001). These procedures improved image contrast, and enabled to provide quantitative image that are equivalent to PET (y(ml/100 g/min)$=1.07\times$ (ml/100 g/min)$-$ 1.14, $r=0.94$).

In conclusion, CBF can be quantified by means of split-dose administration of IMP using SPECT. Contribution of the background radioactivity attributed to the previous administration of radiotracer can be built into the model, with minimal enhancement of statistical noise. The estimated CBF appeared to be most sensitive to the transient CBF immediately after the IMP injection but not to later periods, thus allowing the pharmacological challenges even during the first SPECT scan. Repeat quantitation of CBF could be feasible with considerably shorter intervals than with previous approaches. Accuracy of this approach was sufficiently high and may be of use for clinical studies.

Acknowledgment

This study was supported by the Program for Promotion of Fundamental Studies in Health Science of the Organization for Pharmaceutical Safety and Research (of Japan).

References

Chmielowska, J., Coghill, R.C., Maisog, J.M., Carson, R.E., Herscovitch, P., Honda, M., Chen, R., Hallett, M., 1998. Positron emission tomography [^{15}O]water studies with short interscan interval for single-subject and group analysis: influence of background subtraction. J. Cereb. Blood Flow Metab. 18, 433–443.

Chmielowska, J., Coghill, R.C., Carson, R.E., Ishii, K., Chen, R., Hallett, M., Herscovitch, P., 1999. Comparison of PET [^{15}O] water studies with 6-minute and 10-minute interscan intervals: single-subject and group analyses. J. Cereb. Blood Flow Metab. 19, 570–582.

Hashikawa, K., Matsumoto, M., Moriwaki, H., Oku, N., Okazaki, Y., Uehara, T., Handa, N., Kusuoka, H., Kamada, T., Nishimura, T., 1994. Split dose iodine-123-IMP SPECT: sequential quantitative regional cerebral blood flow change with pharmacological intervention. J. Nucl. Med. 35, 1226–1233.

Hatazawa, J., Iida, H., Shimosegawa, E., Sato, T., Murakami, M., Miura, Y., 1997. Regional cerebral blood flow measurement with iodine-123-IMP autoradiography: normal values, reproducibility and sensitivity to hypoperfusion. J. Nucl. Med. 38, 1102–1108.

Hattori, N., Yonekura, Y., Tanaka, F., Fujita, T., Wang, J., Ishizu, K., Okazawa, H., Tamaki, N., Konishi, J., 1996. One-day protocol for cerebral perfusion reserve with acetazolamide. J. Nucl. Med. 37, 2057–2061.

Hayashida, K., Tanaka, Y., Hirose, Y., Kume, N., Iwama, T., Miyake, Y., Ishida, Y., Matsuura, H., Miyake, Y., Nishimura, T., 1996. Vasoreactive effect of acetazolamide as a function of time with sequential PET ^{15}O-water measurement. Nucl. Med. Commun. 17, 1047–1051.

Hayashida, K., Fukuchi, K., Hasegawa, Y., Kume, N., Cho, I.H., Nishimura, T., 1999. Viable tissue in an area of severely reduced perfusion demonstrated with I-123 iomazenil brain SPECT imaging of benzodiazepine receptors. Clin. Nucl. Med. 24, 576–578.

Hudson, H.M., Larkin, R.S., 1994. Accelerated image reconstruction using ordered subsets of projection data. IEEE Trans. Med. Imaging 13, 601–609.

Iida, H., Kanno, I., Miura, S., Murakami, M., Takahashi, K., Uemura, K., 1986. Error analysis of a quantitative cerebral blood flow measurement using $H_2^{15}O$ autoradiography and positron emission tomography, with respect to the dispersion of the input function. J. Cereb. Blood Flow Metab. 6, 536–545.

Iida, H., Higano, S., Tomura, N., Shishido, F., Kanno, I., Miura, S., Murakami, M., Takahashi, K., Sasaki, H., Uemura, K., 1988. Evaluation of regional differences of tracer appearance time in cerebral tissues using [^{15}O] water and dynamic positron emission tomography. J. Cereb. Blood Flow Metab. 8, 285–288.

Iida, H., Kanno, I., Miura, S., Murakami, M., Takahashi, K., Uemura, K., 1989. A determination of the regional brain/blood partition coefficient of water using dynamic positron emission tomography. J. Cereb. Blood Flow Metab. 9, 874–885.

Iida, H., Kanno, I., Miura, S. (Eds.), 1991. Rapid Measurement of Cerebral Blood Flow with Positron Emission Tomography. Exploring the Brain Functional Anatomy with Positron Tomography. John Wiley & Sons, Chichester.

Iida, H., Itoh, H., Bloomfield, P.M., Munaka, M., Higano, S., Murakami, M., Inugami, A., Eberl, S., Aizawa, Y., Kanno, I., Uemura, K., 1994a. A method to quantitate cerebral blood flow using a rotating gamma camera and iodine-123 iodoamphetamine with one blood sampling. Eur J. Nucl. Med. Mol. Imaging 21, 1072–1084.

Iida, H., Itoh, H., Nakazawa, M., Hatazawa, J., Nishimura, H., Onishi, Y., Uemura, K., 1994b. Quantitative mapping of regional cerebral blood flow using iodine-123-IMP and SPECT. J. Nucl. Med. 35, 2019–2030.

Iida, H., Akutsu, T., Endo, K., Fukuda, H., Inoue, T., Ito, H., Koga, S., Komatani, A., Kuwabara, Y., Momose, T., Nishizawa, S., Odano, I., Ohkubo, M., Sasaki, Y., Suzuki, H., Tanada, S., Toyama, H., Yonekura, Y., Yoshida, T., Uemura, K., 1996. A multicenter validation of regional cerebral blood flow quantitation using [^{123}I]iodoamphetamine and single photon emission computed tomography. J. Cereb. Blood Flow Metab. 16, 781–793.

Iida, H., Narita, Y., Kado, H., Kashikura, A., Sugawara, S., Shoji, Y., Kinoshita, T., Ogawa, T., Eberl, S., 1998. Effects of scatter and attenuation correction on quantitative assessment of regional cerebral blood flow with SPECT. J. Nucl. Med. 39, 181–189.

Iida, H., Watabe, H., Shidahara, M., Kim, K.M., Ogura, T., 2000. Modeling strategy for background compensation in repeat cerebral blood flow quantitation with diffusible tracers. IEEE Med. Img. Conf. Proc. 2, 34–39.

Imaizumi, M., Kitagawa, K., Hashikawa, K., Oku, N., Teratani, T., Takasawa, M., Yoshikawa, T., Rishu, P., Ohtsuki, T., Hori, M., Matsumoto, M., Nishimura, T., 2002. Detection of misery perfusion with split-dose 123I-iodoamphetamine single-photon emission computed tomography in patients with carotid occlusive diseases. Stroke 33, 2217–2223.

Kanno, I., Iida, H., Miura, S., Murakami, M., Takahashi, K., Sasaki, H., Inugami, A., Shishido, F., Uemura, K., 1987. A system for cerebral blood flow measurement using an $H_2^{15}O$ autoradiographic method and positron emission tomography. J. Cereb. Blood Flow Metab. 7, 143–153.

Kim, K.M., Watabe, H., Shidahara, M., Ishida, Y., Iida, H., 2001. SPECT collimator dependency of scatter and validation of transmission dependent scatter compensation methodologies. IEEE Trans. Nucl. Sci. 48, 689–696.

Kudomi, N., Hayashi, T., Teramoto, N., Watabe, H., Kawachi, N., Ohta, Y., Kim, K.M., Iida, H., 2005. Rapid quantitative measurement of $CMRO_2$ and CBF with the dual administration of ^{15}O-labeled oxygen and water during a single PET scan—A validation study with error analysis in anesthetized monkeys. J. Cereb. Blood Flow Metab. 25, 1209–1224.

Kuhl, D.E., Barrio, J.R., Huang, S.C., Selin, C., Ackermann, R.F., Lear, J.L., Wu, J.L., Lin, T.H., Phelps, M.E., 1982. Quantifying local cerebral blood flow by *N*-isopropyl-*p*-[^{123}I]iodoamphetamine (IMP) tomography. J. Nucl. Med. 23, 196–203.

Kurisu, R., Ogura, T., Takikawa, S., Saito, H., Nakazawa, M., Iida, H., 2002. Estimation and optimization of the use of standard arterial input function for split-dose administration of *N*-isopropyl-*p*[^{123}I]iodoamphetamine. Kaku Igaku 39, 13–20.

Lear, J.L., Ackermann, R.F., Kameyama, M., Kuhl, D.E., 1982. Evaluation of [^{123}I]isopropyliodoamphetamine as a tracer for local cerebral blood flow using direct autoradiographic comparison. J. Cereb. Blood Flow Metab. 2, 179–185.

Meikle, S.R., Hutton, B.F., Bailey, D.L., 1994. A transmission-dependent method for scatter correction in SPECT. J. Nucl. Med. 35, 360–367.

Mintun, M.A., Raichle, M.E., Martin, W.R., Herscovitch, P., 1984. Brain oxygen utilization measured with O-15 radiotracers and positron emission tomography. J. Nucl. Med. 25, 177–187.

Narita, Y., Eberl, S., Iida, H., Hutton, B.F., Braun, M., Nakamura, T., Bautovich, G., 1996. Monte Carlo and experimental evaluation of accuracy and noise properties of two scatter correction methods for SPECT. Phys. Med. Biol. 41, 2481–2496.

Nishizawa, S., Iida, H., Tsuchida, T., Ito, H., Konishi, J., Yonekura, Y., 2003. Validation of the Dual-Table autoradiographic method to quantify two sequential rCBFs in a single SPET session with *N*-isopropyl-[^{123}I] *p*-iodoamphetamine. Eur J. Nucl. Med. Mol. Imaging 30, 943–950.

Oku, N., Matsumoto, M., Hashikawa, K., Moriwaki, H., Okazaki, Y., Seike, Y., Handa, N., Uehara, T., Kamada, T., Nishimura, T., 1994. Carbon dioxide reactivity by consecutive technetium-99m-HMPAO SPECT in patients with a chronically obstructed major cerebral artery. J. Nucl. Med. 35 (1), 32–40.

Powers, W.J., 1991. Cerebral hemodynamics in ischemic cerebrovascular disease. Ann. Neurol. 29, 231–240.

Powers, W.J., Raichle, M.E., 1985. Positron emission tomography and its application to the study of cerebrovascular disease in man. Stroke 16, 361–376.

Silbersweig, D.A., Stern, E., Frith, C.D., Cahill, C., Schnorr, L., Grootoonk, S., Spinks, T., Clark, J., Frackowiak, R., Jones, T., 1993. Detection of thirty-second cognitive activations in single subjects with positron emission tomography: a new low-dose $H_2^{15}O$ regional cerebral blood flow three-dimensional imaging technique. J. Cereb. Blood Flow Metab. 13, 617–629.

Silbersweig, D.A., Stern, E., Schnorr, L., Frith, C.D., Ashburner, J., Cahill, C., Frackowiak, R.S., Jones, T., 1994. Imaging transient, randomly occurring neuropsychological events in single subjects with positron emission tomography: an event-related count rate correlational analysis. J. Cereb. Blood Flow Metab. 14, 771–782.

The-EC/IC-Bypass-Study-Group, 1985a. Failure of extracranial–intracranial arterial bypass to reduce the risk of ischemic stroke. Results of an international randomized trial. N. Engl. J. Med. 313, 1191–1200.

The-EC/IC-Bypass-Study-Group, 1985b. The international cooperative study of extracranial/intracranial arterial anastomosis (EC/IC bypass study): methodology and entry characteristics. Stroke 16, 397–406.

Vortrup, S., Henriksen, L., Paulson, O.B., 1984. Effect of acetazolamide on cerebral blood flow and cerebral metabolic rate of oxygen. J. Clin. Invest. 74, 1634–1639.

Vortrup, S., Brun, B., Lassen, N.A., 1986. Evaluation of the cerebral vasodilatory capacity by the acetazolamide test before EC-IC bypass surgery in patients with occlusion of the internal carotid artery. Stroke 17, 1291–1298.

Watabe, H., Kondoh, Y., Kim, K.M., Shidahara, M., Iida, H. (Eds.), 2002. Shortening rCBF Measurement Interval in [^{15}O]H2O PET. Brain Imaging Using PET. Academic Press, San Diego.

Yamaguchi, T., Kanno, I., Uemura, K., Shishido, F., Inugami, A., Ogawa, T., Murakami, M., Suzuki, K., 1986. Reduction in regional cerebral metabolic rate of oxygen during human aging. Stroke 17, 1220–1228.

doi:10.1093/brain/awh702 Brain (2006), 129, 399–410

The association between the Val158Met polymorphism of the catechol-O-methyl transferase gene and morphological abnormalities of the brain in chronic schizophrenia

Takashi Ohnishi,[1,2,4] Ryota Hashimoto,[2] Takeyuki Mori,[1,2] Kiyotaka Nemoto,[1] Yoshiya Moriguchi,[1] Hidehiro Iida,[4] Hiroko Noguchi,[2] Tetsuo Nakabayashi,[2,3] Hiroaki Hori,[2,3] Mayu Ohmori,[3] Ryoutaro Tsukue,[3] Kimitaka Anami,[3] Naotugu Hirabayashi,[3] Seiichi Harada,[3] Kunimasa Arima,[3] Osamu Saitoh[3] and Hiroshi Kunugi[2]

[1]Department of Radiology, National Center Hospital of Mental, Nervous and Muscular Disorders, National Center of Neurology and Psychiatry, [2]Department of Mental Disorder Research, National Institute of Neuroscience, National Center of Neurology and Psychiatry, [3]Department of Psychiatry, National Center Hospital of Mental, Nervous, and Muscular Disorders, National Center of Neurology and Psychiatry, Tokyo and [4]Department of Investigative Radiology, Research Institute, National Cardiovascular Center, Osaka, Japan

Correspondence to: Takashi Ohnishi, Department of Radiology, National Center Hospital of Mental, Nervous, and Muscular Disorders, National Center of Neurology and Psychiatry 4-1-1 Ogawa Higashi, Kodaira City, Tokyo, Japan 187-0031
E-mail: tohnishi@hotmail.com

The catechol-O-methyl transferase (COMT) gene is considered to be a promising schizophrenia susceptibility gene. A common functional polymorphism (Val158Met) in the COMT gene affects dopamine regulation in the prefrontal cortex (PFC). Recent studies suggest that this polymorphism contributes to poor prefrontal functions, particularly working memory, in both normal individuals and patients with schizophrenia. However, possible morphological changes underlying such functional impairments remain to be clarified. The aim of this study was to examine whether the Val158Met polymorphism of the COMT gene has an impact on brain morphology in normal individuals and patients with schizophrenia. The Val158Met COMT genotype was obtained for 76 healthy controls and 47 schizophrenics. The diagnostic effects, the effects of COMT genotype and the genotype-diagnosis interaction on brain morphology were evaluated by using a voxel-by-voxel statistical analysis for high-resolution MRI, a tensor-based morphometry. Patients with schizophrenia demonstrated a significant reduction of volumes in the limbic and paralimbic systems, neocortical areas and the subcortical regions. Individuals homozygous for the Val-COMT allele demonstrated significant reduction of volumes in the left anterior cingulate cortex (ACC) and the right middle temporal gyrus (MTG) compared to Met-COMT carriers. Significant genotype-diagnosis interaction effects on brain morphology were noted in the left ACC, the left parahippocampal gyrus and the left amygdala-uncus. No significant genotype effects or genotype-diagnosis interaction effects on morphology in the dorsolateral PFC (DLPFC) were found. In the control group, no significant genotype effects on brain morphology were found. Schizophrenics homozygous for the Val-COMT showed a significant reduction of volumes in the bilateral ACC, left amygdala-uncus, right MTG and left thalamus compared to Met-COMT schizophrenics. Our findings suggest that the Val158Met polymorphism of the COMT gene might contribute to morphological abnormalities in schizophrenia.

Keywords: schizophrenia; polymorphism; COMT; ACC; DLPFC

Abbreviations: ACC = anterior cingulate cortex; COMT = catechol-O-methyl transferase; DLPFC = dorsolateral prefrontal cortex; FDR = false discovery rate; IQ = intelligence quotient; JART = Japanese version of National Adult Reading Test; ROI = region of interest; SPM = statistical parametric mapping; TBM = tensor-based morphometry

Received July 15, 2005. Revised September 21, 2005. Accepted October 27, 2005. Advance Access publication December 5, 2005

Introduction

Schizophrenia is a severe neuropsychiatric disorder with deficits of multiple domains of cognitive functions, volition and emotion. Family and twin studies have provided cumulative evidence for a genetic basis of schizophrenia (Kendler, 1983; McGue *et al.*, 1983; Sullivan *et al.*, 2003); however, identification of the underlying susceptibility loci has been limited. Collective data have suggested that the aetiology of schizophrenia involves the interplay of complex polygenic influences and environmental risk factors operating on brain maturational processes (Harrison *et al.*, 2005).

In vivo neuroimaging studies have demonstrated that brain abnormalities should play an important role in the pathophysiology of schizophrenia. Structural MRI studies have demonstrated relatively consistent brain abnormalities in patients with schizophrenia, such as enlargement of the ventricular system and regional volume decrease in the temporal lobe structures (Gaser *et al.*, 2001; Okubo *et al.*, 2001; Shenton *et al.*, 2001; Davidson and Heinrichs, 2003). Studies with schizophrenics and their healthy siblings demonstrate that even healthy siblings share some of morphological abnormalities observed in schizophrenia (Steel *et al.*, 2002; Gogtay *et al.*, 2003). A recent morphological MR study revealed that a common polymorphism of the brain-derived neurotrophic factor, one of the well-known schizophrenia susceptibility genes, affected the anatomy of the hippocampus and prefrontal cortex (PFC) in healthy individuals (Pezawas *et al.*, 2004). Furthermore, some studies have suggested that environmental factors interact with genetic factors (Cannon *et al.*, 1993; Nelson *et al.*, 2004). For example, obstetric complications are well known non-genetic risk factors of schizophrenia. However, a previous study suggested that obstetric complications might induce brain morphological abnormalities in schizophrenics and their siblings, but not in comparison with subjects at low genetic risk for schizophrenia (Cannon *et al.*, 1993). These facts suggest that genetic factors should have considerable impact on brain morphology in patients with schizophrenia.

Catechol-O-methyl transferase (COMT) is a promising schizophrenia susceptibility gene because of its role in monoamine metabolism (Goldberg *et al.*, 2003; Stefanis *et al.*, 2004; Harrison *et al.*, 2005). A common single nucleotide polymorphism (SNP) of the COMT gene producing an amino acid substitution of methionine (met) to valine (val) at position 108/158 (Val158Met) affects dopamine regulation in the PFC (Palmatier *et al.*, 1999). This polymorphism impacts on the stability of the enzyme, such that the Val-COMT allele has significantly lower enzyme activity than the Met-COMT allele (Weinberger *et al.*, 2001; Chen *et al.*, 2004). Several studies have revealed that the Val-COMT allele is associated with poorer performances, compared to the Met-COMT allele, in cognitive tasks of frontal function such as the Wisconsin Card Sorting Test (WCST) and N-back task (Egan *et al.*, 2001; Weinberger *et al.*, 2001; Goldberg *et al.*, 2003). The underlying mechanism of such behavioural differences may be related to lower prefrontal dopamine levels arising from higher dopamine catabolism mediated by the Val-COMT allele (Chen *et al.*, 2004; Tunbridge *et al.*, 2004).

The results of studies on the association between the Val158Met polymorphism and schizophrenia have, however, been controversial (Daniels *et al.*, 1996; Kunugi *et al.*, 1997; Ohmori *et al.*, 1998; Norton *et al.*, 2002; Galderisi *et al.*, 2005; Ho *et al.*, 2005). The result of a meta-analysis was even more inconclusive (Fan *et al.*, 2005). Such inconsistency was also found in associations between frontal functions and the Val158Met polymorphism (Egan *et al.*, 2001; Weinberger *et al.*, 2001; Goldberg *et al.*, 2003; Ho *et al.*, 2005). The possible morphological changes due to the COMT gene might be present and play a role in susceptibility to schizophrenia and in giving rise to impaired frontal functions. However, morphological changes underlying functional impairments remain to be clarified.

A recent advancement of methods for MR volumetry, such as voxel-based morphometry and deformation-based morphometry [or tensor-based morphometry (TBM)], allows us to explore and analyse brain structures of schizophrenics (Wright *et al.*, 1995; Gaser *et al.*, 2001). Using TBM techniques, we investigated the association between the Val158-Met polymorphism of the COMT gene and brain morphology in normal individuals and patients with schizophrenia. The aim of this study was to clarify whether there are significant genotype and/or genotype-disease interaction effects on brain morphology.

Methods

Subjects

Seventy-six healthy subjects and forty-seven patients with schizophrenia participated in the study. All the subjects were biologically unrelated Japanese. Written informed consent was obtained from all the subjects in accordance with ethical guidelines set by a local ethical committee. All normal subjects were screened using a questionnaire on medical history and excluded if they had neurological, psychiatric or medical conditions that could potentially affect the CNS, such as substance abuse or dependence, atypical headache, head trauma with loss of consciousness, asymptomatic or symptomatic cerebral infarctions detected by T_2-weighted MRI, hypertension, chronic lung

disease, kidney disease, chronic hepatic disease, cancer, or diabetes mellitus. The patients were diagnosed on the basis of DSM-IV criteria, information from medical records and a clinical interview. All patients were stable and/or partially remitted at the time of MR measurement and neuropsychological tests.

According to genotypes, each group (control and schizophrenia) was categorized into three groups; the homozygous Val-COMT group (control: n = 38, two were left-handed, schizophrenia: n = 19, one was left-handed), the Val/Met-COMT group (control: n = 25, three were left-handed, schizophrenia: n = 22, all were right-handed) and the remaining homozygous Met-COMT group (control: n = 13, all were right-handed, schizophrenia: n = 6, all were right-handed). Because of the small number of subjects with homozygous Met-COMT, the Val/Met-COMT and homozygous Met-COMT groups were combined and treated as one group, the Met-COMT carriers. Table 1 shows the characteristics of each group. All groups were of comparable age, gender (χ^2 test, df = 3, P = 0.38) and handedness (χ^2-test, df = 3, P = 0.53). No genotype effects and genotype-diagnosis interaction effects were found in years of education, scores of full scale Intelligence Quotient (IQ) and scores of premorbid IQ [Japanese version of National Adult Reading Test (JART) score], however, patients who had fewer years of education ($P < 0.0001$), had lower scores of both full scale IQ and JART ($P < 0.001$). The duration of illness, medication and hospitalization, the age at disease onset and drug dose (chlorpromazine equivalent) of those homozygous for the Val-COMT did not differ from the Met-COMT carriers.

SNP genotyping

Venous blood was drawn from subjects and genomic DNA was extracted from whole blood according to the standard procedures. The Val158Met polymorphism of the COMT gene (dbSNP accession: rs4680) was genotyped using the TaqMan 5′-exonuclease allelic discrimination assay, described previously (Hashimoto *et al.*, 2004, 2005). Briefly, primers and probes for detection of the SNP are: forward primer 5′-GACTGTGCCGCCATCAC-3′, reverse primer 5′-CAGGCATGCACACCTTGTC-3′, probe 1 5′-VIC-TTTCGCTG-GCGTGAAG-MGB-3′ and probe 2 5′-FAM-CGCTGGCATGAAG-MGB-3′. PCR cycling conditions were: at 95°C for 10 min, 50 cycles of 92°C for 15 s and 60°C for 1 min.

MRI procedures

All MR studies were performed on a 1.5 tesla Siemens Magnetom Vision plus system. A three dimensional (3D) volumetric acquisition of a T_1-weighted gradient echo sequence produced a gapless series of thin sagittal sections using an MPRage sequence (TE/TR, 4.4/11.4 ms; flip angle, 15°; acquisition matrix, 256 × 256; 1 NEX, field of view, 31.5 cm; slice thickness, 1.23 mm).

Image analysis (TBM)

The basic principle of TBM is to analyse the local deformations of an image and to infer local differences in brain structure. In TBM, MRI scans of individual subjects are mapped to a template image with three-dimensional (3D) non-linear normalization routines. Local deformations were estimated by a univariate Jacobian approach. The basic principle of TBM is the same as a method used in a previous report described as deformation-based morphometry (Gaser *et al.*, 2001). Firstly, inhomogeneities in MR images were corrected using a bias correction function in statistical parametric mapping (SPM2), then the corrected image was scalp-edited by masking with a probability image of brain tissue obtained from each image using a segmentation function in SPM2. Using a linear normalization algorithm in SPM2, all brains were resized to a voxel size of 1.5 mm and adjusted for orientation and overall width, length and height (Fig. 1A). Therefore, brains were transformed to the anatomical space of a template brain whose space is based on Talairach space (Talairach and Tournoux, 1988). Subsequent non-linear normalization introduced local deformations to each brain to match it to the same scalp-edited template brain (Fig. 1C). The non-linear transformation was done using the high-dimension-warping algorithm (Ashburner and Friston, 2004). After the high dimensional warping, each image (Fig. 1B) looks similar to the template (Fig. 1C). Figure 2 demonstrated a mean MR image of 76 controls (left) and a mean MR image of 47 schizophrenics after high dimensional warping (Fig. 2). We obtained 3D deformation fields for every brain (Fig. 1D). Each of these 3D deformation fields consists of displacement vectors for every voxel, which describe the 3D displacement needed to locally deform the brain to match it to the template. We calculated the Jacobian determinants to obtain voxel by voxel parametric maps of local volume change relative to the template brain (Fig. 1E). The local Jacobian determinant is a parameter commonly used in continuum mechanics (Gurtin, 1987), which characterizes volume changes, such as local shrinkage or enlargement caused by warping. The parametric maps of Jacobian determinants were analysed using SPM2, which implements a 'general linear model'. To test hypotheses about regional population effects and interaction, data were analysed by an analysis of covariance (ANCOVA) without global normalization. There was no significant difference in age among the four groups, however, patients with schizophrenia, particularly those homozygous for the Val-COMT allele, were older than controls. Therefore, we treated age and years of education and scores of JART as nuisance variables. Since TBM explores the entire brain (grey matter, CSF space and white matter) at once, the search volume of TBM has a large number of voxels and since our interest was in morphological changes in the grey matter and CSF space, we excluded white matter tissue from analyses by using an explicit mask (Fig. 1F). We used $P < 0.001$, corrected for multiple comparisons with false discovery rate (FDR) <0.05 as a statistical threshold. The resulting sets of t values constituted the statistical parametric maps {SPM (t)}. Firstly, we estimated the main effects, the genotype effect in total subjects (the Val/Val-COMT versus the Met-COMT carriers) and the diagnostic effect (schizophrenia versus controls) and then the genotype-diagnosis interaction effect was estimated. Furthermore, the effects of genotypes in each group (controls carrying the Val/Val-COMT gene versus controls carrying the Met-COMT gene and schizophrenics carrying the Val/Val-COMT gene versus schizophrenics carrying the Met-COMT gene) were estimated within the ANCOVA design matrix. Anatomical localization accorded both to MNI coordinates and Talairach coordinates obtained from M. Brett's transformations (www.mrc-cbu.cam.ac.uk/Imaging/mnispace.html) and are presented as Talairach coordinates (Talairach and Tournoux, 1988). Since previous studies have demonstrated the association between the Val158Met polymorphism and the dorsolateral PFC (DLPFC), we applied an additional hypothesis-driven region of interest (ROI) method to test regional population effects in the DLPFC. For this ROI analysis, we used the Wake Forest University PickAtlas (Maldjian *et al.*, 2003) within the ANCOVA design matrix for SPM analysis. We set $P < 0.05$ (uncorrected) with a small volume correction ($P < 0.05$ within the ROI) to assess grey matter volume changes in the DLPFC (Brodmann area 46, 9 and 8).

Table 1 Subject characteristics

	Control Val/Val	Met carriers	Schizophrenia Val/Val	Met carriers	Diagnosis F (P)	Genotype F (P)*	Genotype by diagnosis F (P)
Number of subjects	38	38	19	28			
Gender (M/F)	16 out of 22	14 out of 24	11 out of 8	13 out of 15			
Handedness (R/L)	36 out of 2	35 out of 3	18 out of 1	28 out of 0			
Age (years)	41.47 (13.42)	39.26 (10.6)	45.98 (15.29)	43.05 (10.57)	3.633 (0.059)	1.7 (0.195)	0.21 (0.647)
Education (years)	17 (3.16)	16.06 (2.57)	12.67 (2.43)	13.33 (3.31)	30.855 (<0.0001)	0.047 (0.828)	1.61 (0.208)
Full scale IQ (WAIS-R)	113.42 (12.05)	108.93 (13.58)	80.69 (17.68)	88.958 (22.08)	57.9 (<0.001)	0.29 (0.59)	3.41 (0.068)
JART	78.8 (10.45)	75.42 (13.65)	54.69 (20.74)	62.25 (27.06)	23.366 (<0.001)	0.292 (0.59)	2.014 (0.159)
Wechsler Memory Scale—Revised							
Verbal memory	111.78 (15.001)	111.061 (12.89)	78.0 (21.623)	81.33 (18.57)	86.93 (<0.001)	0.147 (0.702)	0.354 (0.553)
Visual memory	112.1 (8.51)	106.55 (11.99)	74.78 (24.32)	83.29 (20.613)	85.51 (<0.001)	0.204 (0.65)	4.605 (0.03)
General memory	113.31 (13.92)	110.85 (12.22)	74.43 (21.3)	79.33 (19.14)	111.93 (<0.001)	0.135 (0.715)	1.226 (0.27)
Attention/concentration	104.47 (13.25)	102.94 (16.51)	87.79 (19.09)	92.54 (17.38)	16.08 (0.001)	0.228 (0.634)	0.866 (0.14)
Delayed recall	111.88 (15.46)	112.48 (10.08)	77.07 (20.92)	81.21 (19.19)	99.74 (<0.001)	0.52 (0.475)	0.284 (0.59)
WCST (preservative error)	2.5 (3.89)	3.14 (3.90)	12.08 (11.54)	8.52 (10.63)	24.5 (<0.0001)	0.93 (0.34)	1.93 (0.17)
Digit span	11.12 (3.25)	10.77 (3.34)	7.83 (3.93)	9.09 (2.74)	12.165 (0.0007)	0.415 (0.52)	1.28 (0.261)
Onset age			25.38 (10.34)	23.74 (7.992)		0.52	
Duration of illness (years)			19.86 (14.93)	18.84 (9.8)		0.77	
Duration of hospitalization (months)			66 (153.41)	59.59 (91.18)		0.86	
Duration of medication (years)			12.86 (14.21)	16.4 (9.89)		0.29	
Drug dose of typical antipyschotic drugs (mg/day, chlorpromazine equivalent)			617.9 (720.18)	700.38 (752.67)		0.69	
Drug dose of atypical antipyschotic drugs (mg/day, chlorpromazine equivalent)			282.3 (428.29)	340.23 (482.19)		0.66	

Mean (standard deviation); WAIS-R = Wechsler Adult Intelligence Scale—Revised; JART = Japanese version of National Adult Reading Test; WCST = Wisconsin Card Sorting Test.

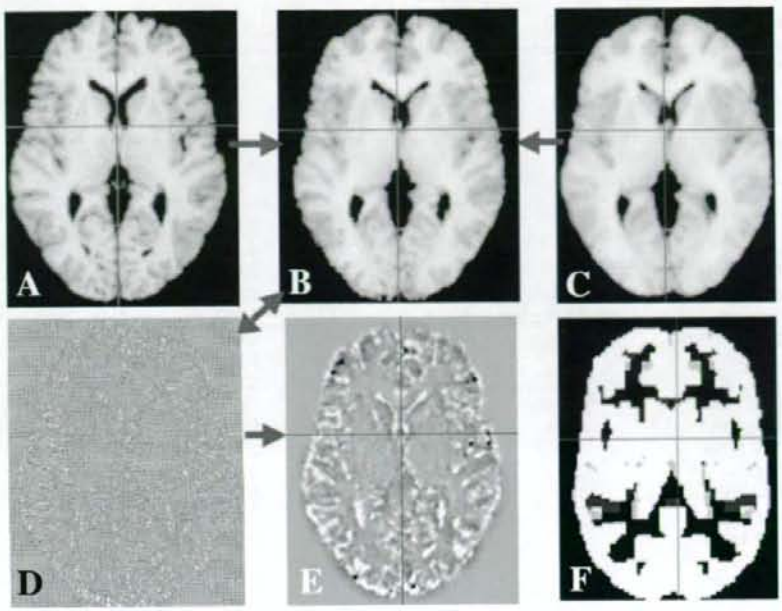

Fig. 1 Steps of analysis for tensor-based morphometry. An example is shown for a single subject in one axial slice. The single object brain (**A**) has been corrected for orientation and overall size to the template brain (**C**). Non-linear spatial normalization removes most of the anatomical differences between the two brains by introducing local deformations to the object brain, which then (**B**) looks as similar as possible to the template. Image (**D**) shows the deformations applied to the object brain by a deformed grid. Statistical analysis can be done univariate using the local Jacobian determinant as a derivative of the field (**E**). An explicit mask image (**F**) was used to explore morphology in the grey matter and CSF space.

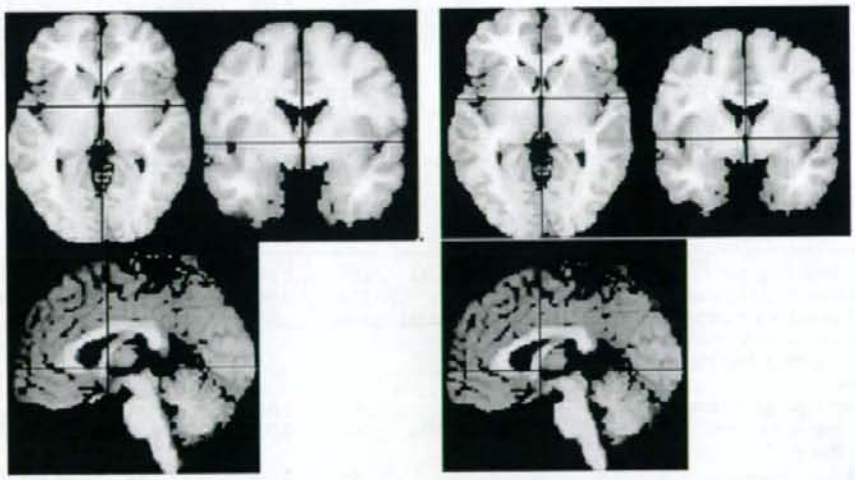

Fig. 2 Mean images after high dimensional warping control subjects and schizophrenics. *Left*: The mean image of warped MR images obtained from 76 controls. Even after averaging, the mean image is not blurred. *Right*: The mean image of warped MR images obtained from 47 schizophrenics. The mean image of schizophrenic looks similar to that of controls.

Results

Behavioural data

Patients had a lower full scale IQ, measured by the Wechsler Adult Intelligence Scale—Revised, than controls. They also had a lower expected premorbid IQ measured by a JART, lower scores of Wechsler Memory Scale—Revised and demonstrated poorer performance of working memory measures such as the number of preservative errors in the WCST and digit span (Table 1). No genotype or genotype-diagnosis interaction effects were found in working memory measures

Table 2 Results of image analyses

Anatomical regions	Brodmann area	Cluster size	Corrected P FDR	T-value (voxel level)	Talairach coordinates		
					x	y	z
Main effects							
Diagnosis effects (control > schizophrenia) (Fig. 3)							
Limbic system							
R insula	BA13	4682	0.000	6.41	33	11	−2
L insula	BA13	4017	0.000	8.81	−33	11	4
R parahippocampal gyrus, amygdala-uncus	BA36	4682	0.000	7.32	30	1	−17
R parahippocampal gyrus	BA36	186	0.000	5.04	30	−41	−8
L parahippocampal gyrus, hippocampus-amygdala	BA34/36	637	0.000	5.46	−20	−41	−8
R anterior cingulate cortex	BA32	147	0.000	4.9	9	33	20
L anterior cingulate cortex	BA32	200	0.000	4.63	−11	32	20
L cingulate gyrus	BA32	275	0.001	4.2	−12	−16	39
Prefrontal cortex							
R inferior frontal gyrus	BA47,11	145	0.000	4.99	27	28	−11
R superior frontal gyrus	BA8/9	1889	0.000	6.08	12	43	39
L medial frontal gyrus	BA9	1333	0.000	5.13	−8	47	19
L inferior frontal gyrus	BA45	141	0.000	4.55	−44	23	15
L middle frontal gyrus	BA8	482	0.000	4.44	−30	24	43
L superior frontal gyrus	BA8	482	0.000	4.39	−35	17	51
Premotor area							
R dorsal premotor area	BA6	429	0.000	4.37	41	13	45
Temporal cortex							
R superior temporal gyrus	BA22	806	0.000	5.04	47	−23	−1
R middle temporal gyrus	BA21	806	0.000	4.87	56	−15	−3
L superior temporal gyrus	BA38	4017	0.000	7	−36	1	−17
Central grey matter							
L thalamus		4017	0.000	7.26	−15	−17	2
Diagnosis effects (control < schizophrenia) (Fig. 4)							
L sylvian fissure		621	0.000	6.7	−45	17	−3
R sylvian fissure		774	0.000	6.59	44	17	−8
Lateral ventricle (anterior horn)		279	0.000	5.27	−5	21	4
Lateral ventricle (L inferior horn)		248	0.000	6.18	−41	−30	−10
Lateral ventricle (R inferior horn)		137	0.000	5.02	36	−40	−1
Interhemisphrenic fissure		154	0.000	5.28	3	55	−12
Genotype effects (Val/Val-COMT < Met-COMT carriers) (Fig. 5)							
Limbic system							
L anterior cingulate cortex	BA24/25	334	0.033	4.29	−8	17	−13
Temporal cortex							
R middle temporal gyrus	BA21	285	0.016	5.10	59	−3	−14
Genotype-diagnosis interaction effects (Fig. 6)							
Limbic system							
L anterior cingulate gyrus	BA24/25/32	264	0.044	3.77	−6	25	−6
L parahippocampal gyrus, amygdala-uncus	BA34	219	0.048	3.74	−24	−6	−14
The effects of polymorphism in control group (no significant difference)							
The effects of polymorphism in schizophrenia Val/Val-COMT < Val/Met, Met/Met-COMT (Fig. 7)							
Limbic system							
L parahippocampal gyrus, amygdala-uncus	BA28	81	0.010	4.17	−26	2	−22
L anterior cingulate cortex	BA24/25/32	263	0.007	4.38	−7	20	−8
Central grey matter							
L thalamus		91	0.014	3.94	−21	−28	6

and IQ, however, a significant genotype-by-diagnosis interaction effect was found in a visual memory measure (F = 4.605, df = 1, P = 0.03) (Table 1). However, a *post hoc* t-test (Bonferroni test) demonstrated no genotype effect in each diagnostic category (control: P = 0.15, schizophrenia: P = 0.11).

Morphological changes in schizophrenia (diagnosis effects)

In comparison with controls, patients with schizophrenia demonstrated a significant reduction of volumes in multiple brain areas, such as the limbic and paralimbic systems, neocortical areas and the subcortical regions (Table 2 and Fig. 3).